

# Strong field-matching effects in superconducting $\text{YBa}_2\text{Cu}_3\text{O}_{7-\delta}$ films with vortex energy landscapes engineered via masked ion irradiation

I. Swiecicki,<sup>1</sup> C. Ulysse,<sup>2</sup> T. Wolf,<sup>3</sup> R. Bernard,<sup>1</sup> N. Bergeal,<sup>3</sup> J. Briatico,<sup>1</sup> G. Faini,<sup>2</sup> J. Lesueur,<sup>3</sup> and Javier E. Villegas<sup>1,\*</sup><sup>1</sup>*Unité Mixte de Physique CNRS/Thales, 1 avenue A. Fresnel, 91767 Palaiseau, and Université Paris Sud, 91405 Orsay, France*<sup>2</sup>*CNRS, Phynano Team, Laboratoire de Photonique et de Nanostructures, route de Nozay, 91460 Marcoussis, France*<sup>3</sup>*LPEM, CNRS-ESPCI, 10 rue Vauquelin 75231 Paris, France*

(Received 29 September 2011; revised manuscript received 12 January 2012; published 4 June 2012)

We have developed a masked ion irradiation technique to engineer the energy landscape for vortices in oxide superconductors. This approach associates the possibility to design the landscape geometry at the nanoscale with the unique capability to adjust the depth of the energy wells for vortices. This enabled us to unveil the key role of vortex channeling in modulating the amplitude of the field matching effects with the artificial energy landscape, and to make the latter govern flux dynamics over an unusually wide range of temperatures and applied fields for high-temperature superconducting films.

DOI: [10.1103/PhysRevB.85.224502](https://doi.org/10.1103/PhysRevB.85.224502)

PACS number(s): 74.25.Wx, 74.78.Na, 74.72.—h

## I. INTRODUCTION

The energy landscape for vortices in superconductors can be engineered via the introduction of ordered distributions of submicrometric structures (e.g., holes or inclusions) that create energy wells (pinning sites) for vortices. This possibility has opened the door to a wide spectrum of fundamental studies, and to a number of applications (for a review, see, e.g., Ref. 1). From the fundamental point of view, the interest of flux dynamics on artificial energy landscapes reaches beyond vortex physics, as it has become a model system to study a variety of problems that involve interacting particles (e.g., colloids, atoms, or charge density waves) moving on a pinning substrate.<sup>2,3</sup> Regarding the technological applications, the ability to manipulate vortices has brought forth the so-called “fluxtronics,” in which vortex confinement, guidance,<sup>4–7</sup> and rectification<sup>8–11</sup> via energy landscapes with special geometries constitute the basis of superconducting diodes,<sup>9–13</sup> signal processing,<sup>14</sup> and novel computing applications.<sup>15–17</sup>

While much of the progress in this area has been done with low critical-temperature ( $T_c$ ) superconductors,<sup>1,2,4,5,8,10,11</sup> extending this research to high- $T_c$  materials<sup>6,7,14,18–23</sup> is particularly interesting. For the latter, the interplay between the artificial ordered pinning, the characteristic anisotropy, and the strong thermal fluctuations predisposes to a richer phenomenology. However, in the presence of strong intrinsic random pinning, the impact of the artificial ordered energy landscape on vortex dynamics—as measured, for example, by the intensity of the field-matching effects observed in the magnetotransport—is generally found to be much weaker in high- $T_c$  (e.g.,  $\text{YBa}_2\text{Cu}_3\text{O}_{7-\delta}$ )<sup>18,19,22,23</sup> than in low- $T_c$  superconductors (e.g., Nb).<sup>1</sup> In addition, the fact that for high- $T_c$  materials those effects are often observed only in a narrow range of temperatures close to  $T_c$ <sup>18,22</sup> casts a shadow on their physical origin. In particular, the possibility that the matching effects arise from Little-Parks oscillations rather than from periodic flux pinning has been earlier discussed.<sup>22</sup>

In this paper we demonstrate that it is possible to induce in  $\text{YBa}_2\text{Cu}_3\text{O}_{7-\delta}$  (YBCO) films field-matching effects which are as strong as in low- $T_c$  superconductors,<sup>1</sup> and we investigate the mechanisms that determine their intensity. We found that the

matching effects observed here are indeed connected to flux pinning and that, in addition to the strength of the individual pinning sites, a more subtle mechanism plays a major role in determining their intensity: vortex channeling across the energy landscape—a phenomenon that critically depends on the distance between pinning sites. The key tool to reach this understanding is the technique we developed to engineer the energy landscape for vortices, which combines e-beam lithography and ion irradiation to “pattern” the local electronic properties of the YBCO via ion damage.<sup>24</sup> Besides the unique capability to adjust the depth of the energy wells, this technique allows shaping the vortex energy landscape with features in the tenths-of-nanometer range. This is about one order-of-magnitude better than achieved by physically patterning high-temperature superconductors via lithography and etching (e.g., introducing arrays of holes).<sup>6,7,9,14,19–21</sup> In addition to the fundamental interest borne by the understanding of the involved physical mechanisms, the obtained results prove our approach a powerful method for vortex manipulation in oxide superconductors, in applied magnetic fields up to two orders of magnitude higher than with other techniques,<sup>6,7,9,14,19–21</sup> and in an unusually wide range of temperatures. This is especially relevant for fluxtronic devices, provided that the vortex density  $n_v$  is directly proportional to the applied magnetic field  $B$ , and consequently higher fields imply greater data storage capacity in devices conceived for logic operation,<sup>15–17</sup> and larger output signals in those for signal processing.<sup>14</sup>

## II. EXPERIMENT

### A. Sample fabrication

The YBCO superconducting thin films (50 nm thick) were grown by pulsed laser deposition on (0 0 1)  $\text{SrTiO}_3$  substrates. Subsequently, multiprobe microbridges for electrical transport measurements were optically lithographed and dry etched [see Fig. 1(a)]. Four separate microbridges were obtained out of the same YBCO film on each single  $\text{SrTiO}_3$  substrate. A second photolithography step—followed by Au sputtering deposition and lift-off—was used to fabricate contact pads to which electrical wires can be ball bonded. In the next step, the samples

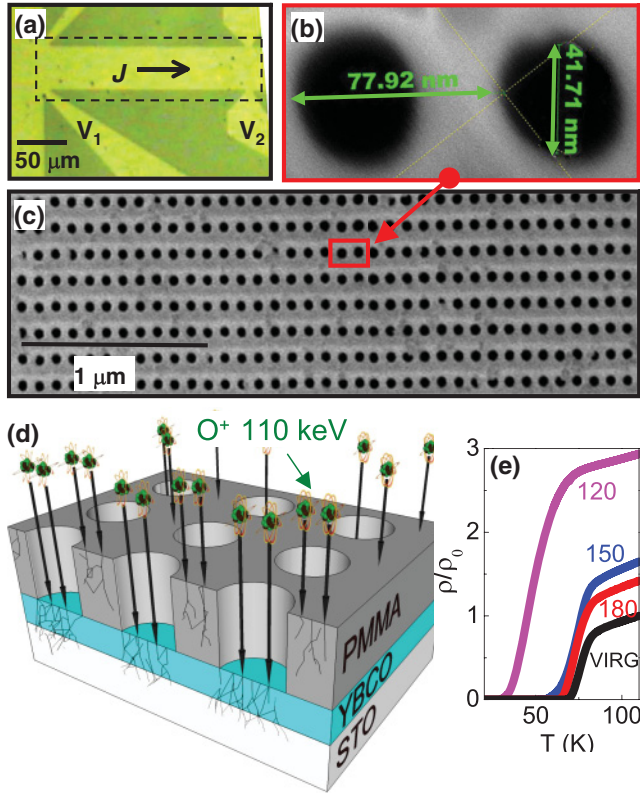


FIG. 1. (Color online) (a) Micrograph of the YBCO microbridge. The voltage contacts ( $V_1$ ,  $V_2$ ) and the current direction flow  $J$  are indicated. The hole array is defined over the rectangular area delimited by dashed lines. (b) Scanning electron microscopy of a PMMA mask. (c) Zoom of the indicated area. (d) Sketch of the ion irradiation of YBCO through a PMMA mask. (e) Resistivity vs temperature of a series of YBCO films, in the virgin state (VIRG) and after irradiation with (energy  $E = 110$  keV and fluence  $f = 5 \times 10^{13}$ ) through masks having different interhole distance  $d$  (see legend, in nm). Curves are normalized to the resistivity of the virgin film at 100 K,  $\rho_0 = 5.63 \times 10^{-4}$   $\Omega$  cm.

were covered with a thick ( $t_{\text{PMMA}} \sim 800$  nm) resist for e-beam lithography (PMMA). This lithography process allowed us to create periodic hole arrays in the PMMA [see Figs. 1(b) and 1(c)], with the desired geometry (square, rectangular, etc), distance between holes  $d$  (center to center), ranging from 80 to 180 nm, and holes diameter  $\emptyset$ . The experiments in this paper are for square arrays of holes with fixed  $\emptyset = 40$  nm and variable  $d = 120, 150,$  and  $180$  nm. The hole arrays were defined over an area of the YBCO microbridges in which these are  $40 \mu\text{m}$  wide and voltage contacts ( $V_1, V_2$ ) are separated  $200 \mu\text{m}$  apart [see Fig. 1(a)]. The arrays were aligned so that their principal axes (sides of the square unit cell) are parallel/perpendicular to the electrical current flow. After e-beam lithography, the resulting nanoporated PMMA layer on top of the YBCO microbridges was used as a mask [Fig. 1(d)] through which we irradiated with  $\text{O}^+$  ions (energy  $E = 110$  keV and fluence ranging  $f = 10^{13}$  to  $5 \times 10^{13}$   $\text{cm}^{-2}$ ). The samples surface was aligned perpendicular to the ion beam with a nominal precision of  $\pm 1$  deg ( $\pm 1.74 \times 10^{-2}$  rad). Although the aspect ratio of the mask holes  $\emptyset/t_{\text{PMMA}} \sim 5 \times 10^{-2}$  is comparable to that number, earlier irradiation experiments<sup>22</sup> performed

with the same ion-beam alignment precision allowed us to efficiently ion-irradiate YBCO films through much thicker porous alumina masks, for which the holes aspect ratio was  $\sim 10^{-3}$ . This suggests that the ion-beam alignment should not be an issue in the present experiments. In fact, as we show below (see Sec. II C), the excellent agreement between the experimental  $T_c$  dependence on the irradiation fluence  $f$  and that expected from theoretical simulations (Sec. II B) implies that the nominal number of  $\text{O}^+$  ions (fluence  $f$ ) reaches the YBCO surface though the PMMA mask holes. In other words, in our experiments there is no significant reduction of the number of  $\text{O}^+$  reaching the YBCO surface due to ion-beam misalignment with respect to the mask holes. Note finally that the microbridges  $T_c$  and the normal-state resistivity  $\rho_N$  do not only depend on the irradiation fluence  $f$ , but also on the distance  $d$  between holes in the mask array. This can be seen in Fig. 1(e), in which the resistance versus temperature  $R(T)$  for a set of YBCO microbridges irradiated with fixed fluence  $f$  through different masks reveal a gradual depression of  $T_c$  and an increase of  $\rho_N$  as  $d$  is decreased. Crucially, all of the YBCO microbridges compared in Fig. 1(e) were obtained from the same YBCO film on a single  $\text{SrTiO}_3$  substrate, which was kept in one piece so as to irradiate all of them at once in strictly identical conditions. This further ensures that random ion-beam misalignment during irradiation and other spurious effects (such as a disparity of the pristine YBCO films properties) do not affect the comparison. As we show in Sec. II C, the behavior in Fig. 1(e) is also understood from the ion damage simulations described below.

## B. Simulations of the irradiation-induced damage

The projected range of penetration of the 110 keV  $\text{O}^+$  ions into PMMA is  $\sim 600$  nm (obtained from Monte Carlo simulations).<sup>25</sup> Therefore the ions are fully stopped by the mask and reach the YBCO film only through the mask holes. The  $\text{O}^+$  ion bombardment does not change the YBCO surface morphology,<sup>22</sup> but creates point defects within the bulk of the material.<sup>21</sup> Since the  $\text{O}^+$  track length into YBCO ( $\sim 150$  nm)<sup>25</sup> is much longer than the film thickness (50 nm), the ion-induced damage within the films is expected in depth from the exposed surface, down into the  $\text{SrTiO}_3$  substrate. The local density of point defects  $\sigma$ —defined as the ratio of displaced atoms per existing ones—can be calculated via Monte Carlo simulations<sup>25</sup> that take into account the irradiation energy  $E$ , the fluence  $f$ , and the PMMA mask geometry.  $\sigma$  (averaged over the film thickness) for different distance between mask holes  $d$  and fluence  $f$  are shown as contour plots in Figs. 2(d)–2(h). Note that the irradiation-induced point defects appear not only underneath the hole areas directly exposed to the ion beam, but also in between these, because the ions spread out as they impinge on the YBCO film. The density of defects in the unexposed areas of the film strongly depends on  $f$  and  $d$ . The presence of point defects implies a local depression of the critical temperature, according to an Abrikosov-Gorkov depairing law.<sup>26</sup> This allows us to calculate the *local* critical temperature  $t_c$  expected from  $\sigma$ .  $t_c(x)$  [with  $x$  the position along the dashed lines shown in Figs. 2(d)–2(f)] is displayed in Figs. 2(a)–2(c). For the highest  $f = 5 \times 10^{13}$   $\text{cm}^{-2}$  [black curves in Figs. 2(a)–2(c)],  $t_c$  is completely suppressed in

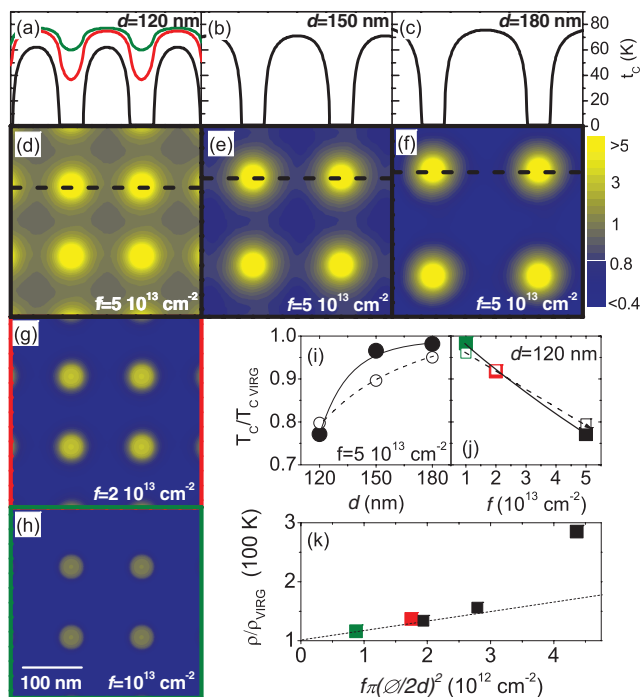


FIG. 2. (Color online) (a)–(c) Local critical temperature  $t_c$  along the array axes indicated by the dashed lines in (d)–(f). Black curves for  $f = 5 \times 10^{13} \text{ cm}^{-2}$ , middle (red) for  $2 \times 10^{13} \text{ cm}^{-2}$ , and top (green) for  $f = 10^{13} \text{ cm}^{-2}$ . (d)–(h) Defect density  $\sigma$  from Monte Carlo simulations for the parameters  $d$  and  $f$  indicated. The color grade is in logarithmic scale (the legend must be multiplied by  $10^{-3}$ ) and saturates above  $5 \times 10^{-3}$  and below  $4 \times 10^{-4}$ . (i) and (j) Superconducting critical temperature after irradiation (normalized to that of the virgin film,  $T_{c,VIRG}$ ) (i) as a function of the array parameter  $d$  (for fixed fluence  $f = 5 \times 10^{13} \text{ cm}^{-2}$ ) and (j) as a function of  $f$  (for fixed  $d = 120 \text{ nm}$ ). Solid symbols are experimental data and hollow ones correspond to the values expected from simulations. (k) Experimental normal-state resistivity of the irradiated samples (at 100 K), normalized to that of the virgin films ( $\rho_0$ ) as a function  $f/d^2$ . The lines are a guide to the eye.

the hole areas directly exposed to the ion beam. Lower  $f$  imply a depressed but finite  $t_c$  in the hole areas [see middle (red) and top (green) curves in Fig. 2(a) for  $2 \times 10^{13}$  and  $10^{13} \text{ cm}^{-2}$ , respectively). Thus, tuning of  $f$  and  $d$  enables us to tailor the spatial modulation of  $t_c$ . Because it is energetically favorable for flux quanta to locate in regions with depressed  $t_c$ ,<sup>27</sup> that allows us to design the vortex energy landscape with nanometric resolution. The potential energy wells for vortices will be formed in areas where  $t_c$  is more substantially depressed (i.e., the circular areas exposed to the ion beam).

### C. Experimental critical temperature and resistivity of the irradiated samples

A comparison between the critical temperatures  $T_c$  expected from the above simulations and the experimental ones is made in Figs. 2(i) and 2(j), as a function  $d$  and  $f$ . The experimental  $T_c$ —onset of the superconducting transition—after irradiation (solid symbols) is defined by  $R(T_c) = 0.9R_N$ , with  $R_N$  the normal-state resistance at the point in which the  $R(T)$  deviates from the linear behavior [see Fig. 1(e)]. Data are normalized

to each of the virgin films' critical temperature, which was around  $T_{c,VIRG} \sim 80\text{--}85 \text{ K}$  in all cases. For each  $d$  and  $f$  we considered that the onset of the superconducting transition ( $T_c$ ) expected from the simulations [represented by hollow symbols in Figs. 2(i) and 2(j)] corresponds to the maximum local  $t_c$  in the area not directly exposed to the ion beam (i.e., in between the mask holes). One can see that the experimental dependences of  $T_c$  on  $d$  [Fig. 2(i)] and on  $f$  [Fig. 2(j)] are well reproduced by the  $T_c(d)$  and  $T_c(f)$  expected from the simulations (hollow symbols in the same figures), both qualitatively and quantitatively. As discussed above, this implies that the number of ions actually reaching the YBCO surface through the mask holes is essentially the nominal one, given by  $f$ . Furthermore, the agreement between the experimental  $T_c$  and the ones obtained from simulations suggests that the latter rightfully predict the defect density distribution and spatial  $t_c$  modulation induced by the masked ion irradiation.

The increase of the normal-state resistivities experimentally observed for ion-irradiated samples are displayed in Fig. 2(k) as a function of  $f\pi(\varnothing/2d)^2$ —the “average irradiation dose.” The resistivities are calculated from the resistances measured at 100 K, taking into consideration the films thickness and the microbridge dimensions. In the graph the irradiated samples resistivity is normalized to that of the unirradiated films (in the range  $\rho_0 \sim 500\text{--}700 \mu\Omega \text{ cm}$  in all cases). Note that the resistivity scales with  $f\pi(\varnothing/2d)^2$ , but it is not directly proportional to it at high doses. This is as expected considering that the ion damage is inhomogeneous and mainly localized underneath the mask holes. At high doses, the resistivity in these regions can be orders-of-magnitude higher than in the unexposed areas,<sup>24</sup> and therefore the current mainly flows along the latter. This results in a reduction of the samples effective section, and thus in an enhanced resistance. A more elaborated model that takes these effects into account would be required for a quantitative analysis of the samples resistivity, which is not the scope of this paper.

## III. RESULTS AND DISCUSSION.

Figures 3(a)–3(f) depict the resistance versus applied field  $B$ ,  $R(B)$ , for different  $d$  and  $f$  [each panel correspond to one of the cases for which the irradiation simulations are shown in Figs. 2(d)–2(h)]. Note that the resistance is defined as  $R \equiv V/I$ , with  $V$  the measured voltage and  $I$  the injected current (the same definition applies for Figs. 4 and 5).  $B$  is applied perpendicular to the film plane, and the current is injected parallel to one of the energy landscape's main axis [see sketch in Fig. 3(a)]. For each sample, the magnetoresistance was measured for a number of different temperatures and current levels  $J$  (some examples of data sets are shown in Fig. 4). In order to be able to perform comparisons between the different samples, we selected for Figs. 3(a)–3(e) measurements done with the same current  $J$  [the latter being low enough to ensure it lays within the range in which the samples' response is Ohmic, in particular in the low-current Ohmic regime above the irreversibility line,<sup>27</sup> as seen in Figs. 4(c) and 4(d) for two of the samples]. We chose the temperatures with the criterion that all of the samples display similar zero-field resistance normalized to the normal-state one  $R_N$ , that is, similar  $R(B = 0)/R_N$ . This criterion ensures that we compare curves

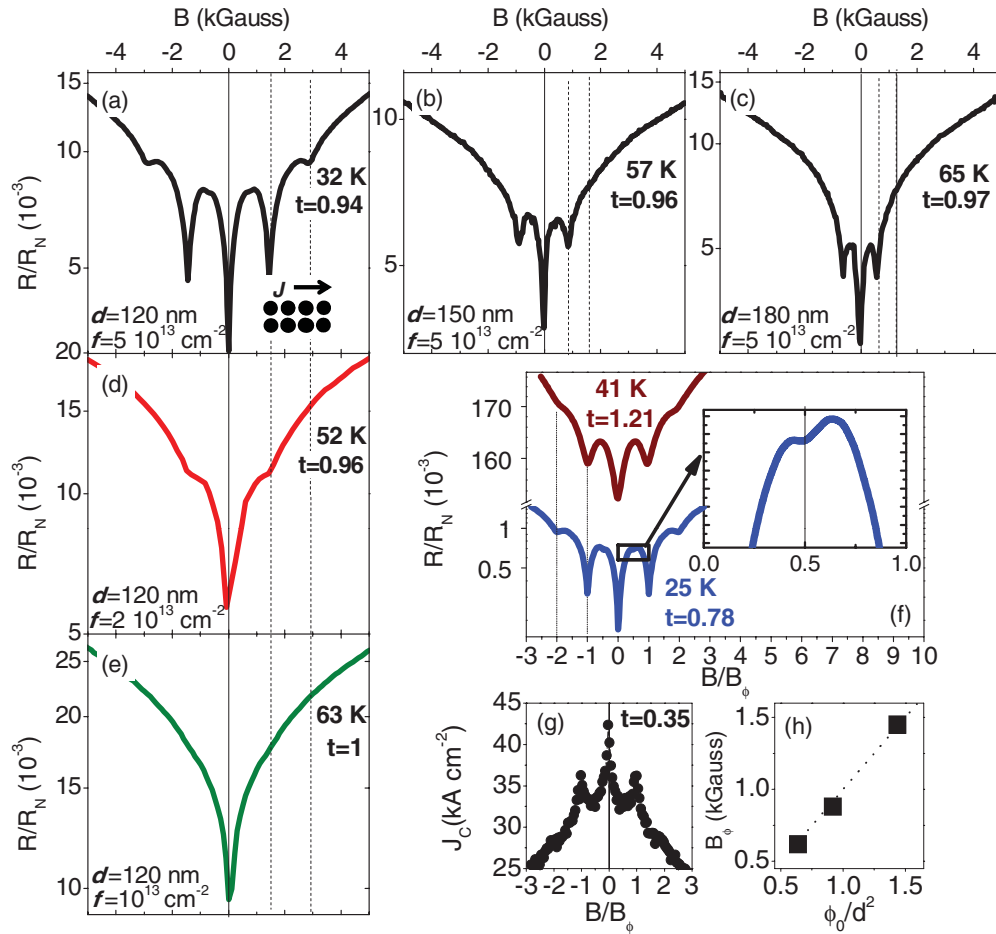


FIG. 3. (Color online) (a)–(e) Mixed-state resistance (normalized to the normal-state one  $R_N$ ) as a function of the applied field  $B$ , different  $d$  and  $f$  (see legends). The injected current was  $J = 0.5$  kA cm $^{-2}$ . The vertical dashed lines mark the first and second order matching fields. (f) Same as in (a) at two different temperatures and  $J = 2.5$  kA cm $^{-2}$ .  $B_\phi = 1.45$  kG is the matching field. Inset: zoom of the curve. (g) Critical current as a function of the applied field for the same sample as in (a) at  $T = 12$  K ( $t = 0.35$ ) (h) Experimental matching fields  $B_\phi$  as a function of  $\phi_0/d^2$ .

measured equally far from the normal state. Note that if one defines  $T_{c0}$  as the temperature at which  $R(T_{c0}) = 10^{-2} R_N$  in zero field, for the curves displayed in Figs. 3(a)–3(e) the above resistance criterion is equivalent to selecting for comparison  $R(B)$  curves measured at a reduced temperature near  $t \equiv T/T_{c0} \sim 1$  (the exact  $t$  is indicated in each panel).

A series of pronounced periodic oscillations are observed in the curves (note that the y axis is in logarithmic scale). The amplitude of the magnetoresistance oscillations decreases with increasing spacing  $d$  [for fixed  $f$ , Figs. 3(a)–3(c)], and also when the  $f$  is decreased [for fixed  $d$ , Figs. 3(a)–3(e)]. For each curve, the more pronounced minima correspond to the “matching field”  $B = \pm B_\phi$ , with  $B_\phi \approx B_1 \equiv \phi_0/d^2$  the field at which the external field induces one flux quantum per unit cell of the square array. The good agreement between the experimental  $B_\phi$  and the expected matching field  $\phi_0/d^2$  is demonstrated in Fig. 3(h). The difference between the experimental  $B_\phi$  and  $\phi_0/d^2$  ranges for all of the samples between 1% and 5%. The sample with the highest  $f = 5 \times 10^{13}$  cm $^{-2}$  and shortest  $d = 120$  nm [Figs. 3(a) and 3(f)] presents clear minima also at  $B = \pm 2B_1$  (two flux quanta per unit cell). However, the second-order minima become less

pronounced as  $d$  is increased [Figs. 3(a)→3(b)→3(c)]. For lower  $f$  [Figs. 3(d) and 3(e)], only first-order matching effects are visible. Note finally that a closer look to the curve in Fig. 3(f) (see inset) unveils the presence of fractional matching at  $B = 0.5B_1$ , for which minima are shallower, as expected.<sup>28</sup> In summary, the strongest matching effects (characterized by deeper minima, and the by presence of clearer second order and fractional matching) are observed for the shortest  $d$  and highest  $f$ . Note that this conclusion is valid regardless of the  $R(B = 0)/R_N$  taken in order to select the set of  $R(B)$  curves for comparison. We verified this by selecting and comparing sets of curves at different temperatures, with  $10^{-4} < R(B = 0)/R_N < 10^{-1}$  ( $0.8 < t < 1.2$ ). Note also that the different magnetoresistance behavior depending on  $d$  cannot be ascribed to different irradiation conditions or different YBCO properties since the samples compared as a function of  $d$  were made out of the same YBCO film, and were simultaneously irradiated on the same piece of SrTiO $_3$ .

The commensurability effects described above are the well-known fingerprint of periodic flux pinning in superconductors.<sup>1,4,5,8,10,14,19–21</sup> Matching of the flux lattice to the square geometry of the artificial energy landscape produces

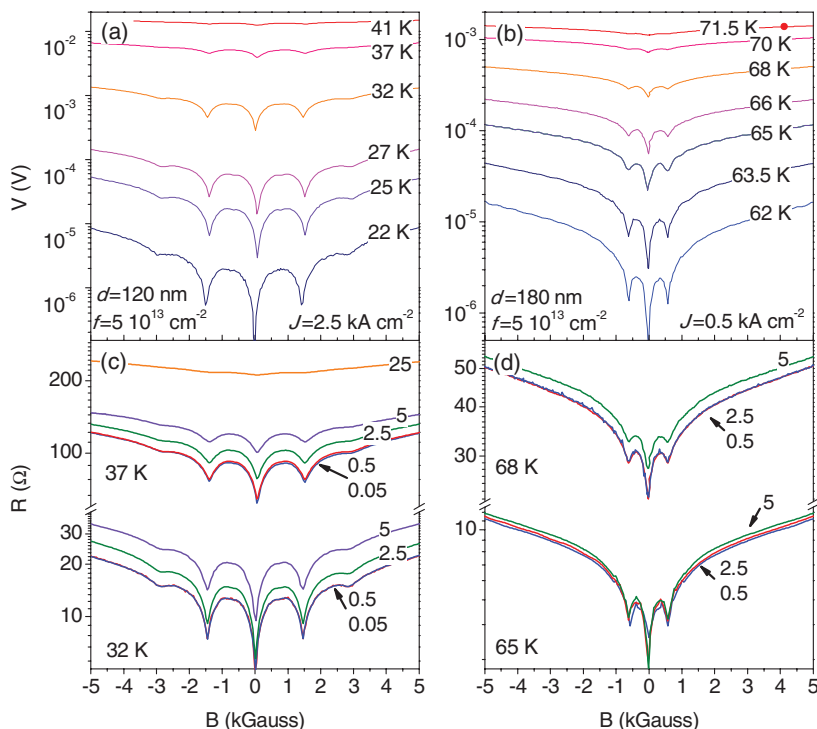


FIG. 4. (Color online) (a) and (b) Voltage as a function of the applied magnetic field  $B$  at fixed injected current density  $J$  (see legend), for different temperatures (indicated on top each curve), respectively for samples with  $d = 120$  nm and  $d = 180$  nm with equal  $f = 5 \times 10^{13}$  cm $^{-2}$ . (c) and (d) Resistance ( $R = V/I$ ) as a function of the applied field  $B$  at two different fixed temperatures (see legend) for different current levels  $J$  (indicated in kA cm $^{-2}$ ), respectively for the same samples as in (a) and (b). For the temperatures shown, the resistance is Ohmic for currents  $J < 2.5$  kA cm $^{-2}$  (c) and  $J < 5$  kA cm $^{-2}$  (d). The lowest temperature for each sample corresponds to that of the measurements in Figs. 3(a)–3(e), which are for  $J = 0.5$  kA cm $^{-2}$  and therefore within the Ohmic regime of the resistance.

a vortex pinning enhancement, which slows down vortex motion and leads to a resistance decrease. The current dependence of the magnetoresistance oscillations is as expected for flux pinning effects: increasing the injected current leads to a smoothing of the magnetoresistance oscillations, as it can be seen in the examples shown in Figs. 4(c) and 4(d). All of the studied samples show the same behavior, which is as expected because the increasing Lorentz force on the vortices—which is proportional to the injected current—gradually washes out the artificial energy landscape effects. Regarding the temperature effects, comparison of magnetoresistance curves measured with the same  $J$  at different temperatures [see examples in Figs. 3(f), 4(a), and 4(b)] shows for all the samples that the commensurability effects gradually smooth out with increasing temperature. Note however that in the present

experiments the matching effects appear in an unusually wide range of temperatures below  $T_c$  as compared to previous work on oxide superconductors.<sup>14,19,20,22,23</sup> In particular, for the samples irradiated with the highest fluence ( $f = 5 \times 10^{13}$  cm $^{-2}$ ), the matching effects are present both above and below the irreversibility line<sup>27</sup> (which was determined from the curvature of  $I(V)$  characteristics). In the latter case, the matching effects are also visible in the critical depinning current  $J_c$  versus field, very far below  $T_c$  [see Fig. 3(g)]. This behavior is unusual in YBCO thin films, for which matching effects are typically found only very close to  $T_c$ <sup>19</sup>—and gradually disappear when temperature is reduced as the disordered intrinsic pinning prevails over the artificial pinning landscape.

The results displayed in Fig. 3 show that the strength of the field-matching effects depends on two parameters. One of them is the irradiation fluence  $f$ , as illustrated by the evolution observed in Figs. 3(a)→3(d)→3(e). This dependence is easily understood: the amplitude of the  $t_c$  modulation diminishes as the irradiation fluence is decreased [Fig. 2(a)], which leads to shallower potential energy wells and thus to weaker flux pinning. The other key parameter is the distance between holes in the mask  $d$ . Interestingly, relatively small variations of the array dimensions produce dramatic changes: for fixed  $f$ , the strength of the matching effects—as measured by the presence or not of second order and fractional matching, and by the amplitude of the magnetoresistance oscillations—steadily decreases as  $d$  is increased [Figs. 3(a)→3(c)]. Note that this is just the contrary to what one could *a priori* expect from simple arguments. First, and considering that the ion damage in the interhole areas not directly exposed to the ion beam is stronger the shorter is  $d$  [see Figs. 2(d)–2(f)], one expects a reduced  $t_c$  contrast—and therefore shallower pinning potential wells and weaker matching effects—for the samples with the shortest  $d$ . This is just opposite of what is observed [Fig. 3(a)].

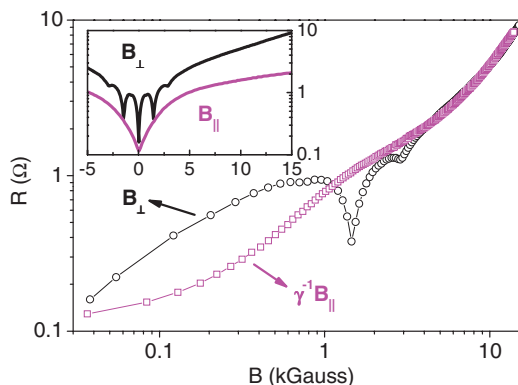


FIG. 5. (Color online) Magnetoresistance with the field applied perpendicular ( $B_{\perp}$ ) and parallel ( $B_{\parallel}$ ) to the  $ab$  plane, for the sample with  $f = 5 \times 10^{13}$  cm $^{-2}$  and  $d = 120$  nm, at  $T = 27$  K ( $t = 0.79$ ) and with  $J = 1.25$  kA cm $^{-2}$ . The inset shows the raw data and the main panel the curves collapse using the anisotropy  $\gamma \sim 4$ .

Second, note that all the measurements compared in Fig. 3 are carried out with the same *overall* injected current  $J$ . However, the shorter is  $d$ , the smaller the cross section of the superconducting interhole areas, and therefore the higher the local current density  $j$  across them. Since as we discussed above the matching effects are progressively washed out as current density increases, from this second argument one also expects the weakest matching effects for samples where  $d$  is the shortest. Again, the observed behavior is just opposite to that. We show below that a more subtle mechanism, flux channeling across the energy landscape,<sup>1,4-7</sup> allows for an understanding of this unexpected behavior.

Vortex channeling has been previously studied in the frame of vortex guidance by anisotropic energy landscapes.<sup>1,4-7</sup> This effect is defined as the preferred motion of vortices along the channels that form in the energy landscape due to the overlapping of the potential energy wells. The shorter the distance between the latter, the wider the overlap between them, and the stronger the channeling effects.<sup>1,4-7</sup> Vortex channeling directs vortex motion along easy-flow directions (for an energy landscape of square geometry, this is along the sides of the square unit cell).<sup>1,4-7</sup> As it was demonstrated in experiments with rectangular arrays of pinning centers in low- $T_c$  superconductors,<sup>29</sup> the stronger the channeling, the weaker the background pinning: the channels are easy-flow “lanes” in the energy landscape, whose presence yield a higher background vortex mobility, particularly for fields in which the flux lattice does not match the pinning potential (i.e., for fields different from  $B = B_1, 2B_1, \dots$ , etc.). Only at the matching fields, in which geometrical coincidence between the flux lattice and the pinning landscape is possible and all the vortices are simultaneously subject to the pinning force from a potential well, the vortex mobility is dramatically reduced, giving rise to minima in the resistance. Thus, in the presence of strong vortex channeling, one expects larger amplitude magnetoresistance oscillations than when channeling is weak, due to a greater difference between the resistances at the matching condition and out-of-matching. This mechanism explains the stronger matching effects for square arrays in which  $d$  is the shortest. Note that, in the present experiments, the  $d$  dependence of the energy wells overlap (the cause of channeling) is exacerbated, because the ion damage—and therefore  $t_C$ —within the areas in between the mask holes strongly depends on  $d$ , as illustrated by Fig. 2. Because of this, small  $d$  variations do dramatically change the intensity of the commensurability effects.

In order to underpin the above scenario, we compared the mixed-state magnetoresistance with the magnetic field applied in plane (i.e., parallel to the  $ab$  plane;  $B_{\parallel}$ ) and out-of-plane (perpendicular to the  $ab$  plane,  $B_{\perp}$ ). This is shown in Fig. 5 for the sample that exhibits the strongest matching effects ( $f = 5 \times 10^{13} \text{ cm}^{-2}$  and  $d = 120 \text{ nm}$ ). The electrical current is perpendicular to the applied field in both cases.

The inset of Fig. 5 shows the raw  $R(B)$ . As expected, the commensurability effects are absent when the applied field is parallel to the film plane: in this case, the Lorentz force is perpendicular to the film plane, and therefore the vortices are forced to move in the direction perpendicular to the artificial periodic energy landscape. The background magnetoresistance is very different depending on the applied field direction. In particular,  $R(B_{\parallel}) \ll R(B_{\perp})$  as is expected for anisotropic

superconductors.<sup>27</sup> We quantitatively analyzed this behavior via the anisotropic Ginsburg-Landau approach.<sup>27</sup> In the absence of artificial pinning, this allows scaling the external field via the anisotropy parameter  $\gamma$  and the rule  $B = \gamma^{-1} B_{\parallel} = B_{\perp}$ , so that  $R(\gamma^{-1} B_{\parallel}) = R(B_{\perp})$ . For pristine YBCO films  $\gamma \sim 5-7$ . For the irradiated film, however, such scaling is not possible over the entire field range, but only for  $B > \sim 5 \text{ kOe}$ . This is shown in the main panel of Fig. 5, which displays the collapse of  $R(\gamma^{-1} B_{\parallel})$  and  $R(B_{\perp})$ , obtained with  $\gamma \sim 4$ . The comparison of  $R(\gamma^{-1} B_{\parallel})$  and  $R(B_{\perp})$  in the field range within which they do not coincide provides us with valuable information. Below the first matching field, when the vortex density is low,  $R(B_{\perp}) < R(\gamma^{-1} B_{\parallel})$ . That is, a higher dissipation is observed when the field is applied perpendicular to the film plane than in plane. This supports the channeling scenario: a higher vortex mobility is observed for out-of-plane than for in-plane fields because in the former case vortices move along the energy landscape channels, while in the latter case there is no channeling because vortices move perpendicularly to the artificial energy landscape. For fields closer to the matching condition ( $B_{\perp} = B_1$ ), the pinning enhancement for perpendicular field dramatically reduces the vortex mobility, and makes the resistance much lower than in parallel field,  $R(B_{\perp}) \ll R(\gamma^{-1} B_{\parallel})$ . According to previous work,<sup>30</sup>  $R(B_{\perp}) \ll R(\gamma^{-1} B_{\parallel})$  at the matching fields (i.e., for  $B = B_1$  and  $2B_1$ ) confirms that the magnetoresistance oscillations are connected to flux pinning phenomena, and rules out that the irradiated film was merely behaving as a superconducting wire network<sup>31</sup> and the oscillatory magnetoresistance originated from Little-Parks<sup>32</sup> or closely related effects<sup>33</sup> (incidentally, this is further supported by the fact that the periodic field modulation can be seen also in  $J_C(B)$  [Fig. 3(g)], at temperatures far below  $T_c$ , contrary to what is observed for flux quantization effects in superconducting wire networks).<sup>33</sup> Finally, in the high field regime  $B > \sim 5 \text{ kOe}$ , even though the commensurability effects are not visible, the presence of the periodic energy landscape produces a somewhat reduced anisotropy ( $\gamma \sim 4$ ) as compared to plain YBCO.

#### IV. CONCLUSIONS

We have developed a masked irradiation technique that allows engineering the energy landscape for flux quanta in high-temperature superconductors. The key ingredient of the present work—as compared to the previous plethora of studies<sup>26,34</sup> on flux pinning induced by ion irradiation—is that here we can design the geometry of the energy landscape at will, with nanometric resolution. This capability allowed us to investigate the mechanisms that determine the intensity of the matching effects between the flux lattice and the artificial energy landscape. By means of experiments in which we changed the lateral dimensions of the energy landscape and the field orientation during magnetotransport measurements, we evidenced the key role played by vortex channeling effects. In particular, we found that the matching effects become more pronounced as the distance between energy wells is shortened, because this increases vortex channeling. Scaling of the energy landscape characteristic lengths down to the tenths-of-nanometer range produces matching effects in YCBO which are as strong as those typically observed for low- $T_c$  superconductors.<sup>1</sup> Furthermore, those effects are

visible in an unusually wide temperature range below  $T_c$ , which so far had been only observed for low-temperature superconductors.<sup>35–37</sup> Ultimately, our results demonstrate the possibility to finely control flux dynamics in fields up to two orders-of-magnitude higher than it has been so far achieved with conventional lithography/etching techniques for pinning arrays in high- $T_c$  films.

We would like to stress before concluding that the energy landscapes produced via irradiation are stable in time: comparison of the magnetotransport of one of the studied samples ( $f = 5 \times 10^{13} \text{ cm}^{-2}$  and  $d = 120 \text{ nm}$ ) right after irradiation and 11 months later (during which the samples

were stored at room temperature in a  $\text{N}_2$  atmosphere) revealed no change in the magnetoresistance behavior. Finally, note that the “electronic patterning” technique used here could be applied, in addition to other oxide superconductors, to a variety of functional oxides sensitive to local disorder (e.g., ferromagnets or semiconductors)<sup>38</sup> in order to engineer phase segregation at the nanoscale.

#### ACKNOWLEDGMENT

Work supported by the French ANR via “SUPERHYBRIDS-II.”

\*javier.villegas@thalesgroup.com

<sup>1</sup>M. Vélaz, J. I. Martin, J. E. Villegas, A. Hoffmann, E. M. Gonzalez, J. L. Vicent, and I. K. Schuller, *J. Magn. Magn. Mater.* **320**, 2547 (2008).

<sup>2</sup>J. E. Villegas, M. I. Montero, C. P. Li, and I. K. Schuller, *Phys. Rev. Lett.* **97**, 027002 (2006).

<sup>3</sup>A. Libal, C. J. O. Reichhardt, and C. Reichhardt, *Phys. Rev. Lett.* **102**, 237004 (2009).

<sup>4</sup>J. E. Villegas, E. M. Gonzalez, M. I. Montero, I. K. Schuller, and J. L. Vicent, *Phys. Rev. B* **68**, 224504 (2003); **72**, 064507 (2005).

<sup>5</sup>A. V. Silhanek, L. Van Look, S. Raedts, R. Jonckheere, and V. V. Moshchalkov, *Phys. Rev. B* **68**, 214504 (2003).

<sup>6</sup>A. Crisan, A. Pross, D. Cole, S. J. Bending, R. Wordenweber, P. Lahl, and E. H. Brandt, *Phys. Rev. B* **71**, 144504 (2005).

<sup>7</sup>R. Wordenweber, E. Hollmann, J. Schubert, R. Kutzner, and A. K. Ghosh, *Appl. Phys. Lett.* **94**, 202501 (2009).

<sup>8</sup>J. E. Villegas, S. Savel'ev, F. Nori, E. M. Gonzalez, J. V. Anguita, R. Garcia, and J. L. Vicent, *Science* **302**, 1188 (2003).

<sup>9</sup>R. Wordenweber, P. Dymashevski, and V. R. Misko, *Phys. Rev. B* **69**, 184504 (2004).

<sup>10</sup>C. D. Silva, J. V. de Vondel, M. Morelle, and V. V. Moshchalkov, *Nature (London)* **440**, 651 (2006).

<sup>11</sup>K. Yu, M. B. S. Hesselberth, P. H. Kes, and B. L. T. Plourde, *Phys. Rev. B* **81**, 184503 (2010).

<sup>12</sup>D. Cole, S. Bending, S. Savel'ev, A. Grigorenko, T. Tamegai, and F. Nori, *Nat. Mater.* **5**, 305 (2006).

<sup>13</sup>S. A. Harrington, J. L. MacManus-Driscoll, and J. H. Durrell, *Appl. Phys. Lett.* **95**, 022518 (2009).

<sup>14</sup>S. Ooi, S. Savel'ev, M. B. Gaifullin, T. Mochiku, K. Hirata, and F. Nori, *Phys. Rev. Lett.* **99**, 207003 (2007).

<sup>15</sup>M. B. Hastings, C. J. O. Reichhardt, and C. Reichhardt, *Phys. Rev. Lett.* **90**, 247004 (2003).

<sup>16</sup>M. V. Milosevic, G. R. Berdiyrov, and F. M. Peeters, *Appl. Phys. Lett.* **91**, 212501 (2007).

<sup>17</sup>M. V. Milosevic and F. M. Peeters, *Appl. Phys. Lett.* **96**, 19 (2010).

<sup>18</sup>J. Y. Lin, M. Gurvitch, S. K. Tolpygo, A. Bourdillon, S. Y. Hou, and J. M. Phillips, *Phys. Rev. B* **54**, 12717 (1996).

<sup>19</sup>A. Castellanos, R. Wordenweber, G. Ockenfuss, A. v.d. Hart, and K. Keck, *Appl. Phys. Lett.* **71**, 962 (1997).

<sup>20</sup>S. Goldberg, Y. Segev, Y. Myasoedov, I. Gutman, N. Avraham, M. Rappaport, E. Zeldov, T. Tamegai, C. W. Hicks, and K. A. Moler, *Phys. Rev. B* **79**, 064523 (2009).

<sup>21</sup>S. Avci, Z. L. Xiao, J. Hua, A. Imre, R. Divan, J. Pearson, U. Welp, W. K. Kwok, and G. W. Crabtree, *Appl. Phys. Lett.* **97**, 042511(2010).

<sup>22</sup>J. E. Villegas, I. Swiecicki, R. Bernard, A. Crassous, J. Briatico, T. Wolf, N. Bergeal, J. Lesueur, C. Ulysse, G. Faini, X. Hallet, and L. Piraux, *Nanotechnology* **22**, 075302 (2011).

<sup>23</sup>A. Crassous, R. Bernard, S. Fusil, K. Bouzehouane, D. Le Bourdais, S. Enouz-Vedrenne, J. Briatico, M. Bibes, A. Barthélémy, and J. E. Villegas, *Phys. Rev. Lett.* **107**, 247002 (2011).

<sup>24</sup>M. Sirena, S. Matzen, N. Bergeal, J. Lesueur, G. Faini, R. Bernard, J. Briatico, and D. G. Crete, *J. Appl. Phys.* **105**, 023910 (2009).

<sup>25</sup>We used “SRIM,” see J. F. Ziegler and J. P. Biersack, *SRIM* (IBM, New York, 2004).

<sup>26</sup>J. Lesueur, P. Nedellec, H. Bernas, J. P. Burger, and L. Dumoulin, *Physica C* **167**, 1 (1990).

<sup>27</sup>G. Blatter, M. V. Feigelman, V. B. Geshkenbein, A. I. Larkin, and V. M. Vinokur, *Rev. Mod. Phys.* **66**, 1125 (1994).

<sup>28</sup>C. Reichhardt and N. Gronbech-Jensen, *Phys. Rev. B* **63**, 054510 (2001).

<sup>29</sup>M. Vélez, D. Jaque, J. I. Martin, M. I. Montero, I. K. Schuller, and J. L. Vicent, *Phys. Rev. B* **65**, 104511 (2003).

<sup>30</sup>U. Patel, Z. L. Xiao, J. Hua, T. Xu, D. Rosenmann, V. Novosad, J. Pearson, U. Welp, W. K. Kwok, and G. W. Crabtree, *Phys. Rev. B* **76**, 020508 (2007).

<sup>31</sup>B. Pannetier, J. Chaussy, R. Rammal, and J. C. Villegier, *Phys. Rev. Lett.* **53**, 1845 (1984).

<sup>32</sup>P. L. Gammel, P. A. Polakos, C. E. Rice, L. R. Harriott, and D. J. Bishop, *Phys. Rev. B* **41**, 2593 (1990).

<sup>33</sup>I. Sochnikov, A. Shaulov, Y. Yeshurun, G. Logvenov, and I. Bozovic, *Nat. Nanotech.* **5**, 516 (2010).

<sup>34</sup>A. Umezawa, G. W. Crabtree, J. Z. Liu, H. W. Weber, W. K. Kwok, L. H. Nunez, T. J. Moran, C. H. Sowers, and H. Claus, *Phys. Rev. B* **36**, 7151 (1987); L. Civale, A. D. Marwick, M. W. McElfresh, T. K. Worthington, A. P. Malozemoff, F. H. Holtzberg, J. R. Thompson, and M. A. Kirk, *Phys. Rev. Lett.* **65**, 1164 (1990); F. M. Sauerzopf, H. P. Wiesinger, W. Kritscha, H. W. Weber, G. W. Crabtree, and J. Z. Liu, *Phys. Rev. B* **43**, 3091 (1991); Y. M. Zhu, Z. X. Cai, R. C. Budhani, M. Suenaga, and D. O. Welch, *ibid.* **48**, 6436 (1993); S. K. Tolpygo, J. Y. Lin, M. Gurvitch, S. Y. Hou, and J. M. Phillips, *ibid.* **53**, 12462 (1996); L. M. Paulius, J. A. Fendrich, W. K. Kwok, A. E. Koshelev, V. M. Vinokur, G. W. Crabtree, and B. G. Glagola, *ibid.* **56**, 913 (1997); S. S. Banerjee, A. Soibel, Y. Myasoedov, M. Rappaport, E. Zeldov, M. Menghini, Y. Fasano,

- F. de la Cruz, C. J. van der Beek, M. Konczykowski, and T. Tamegai, *Phys. Rev. Lett.* **90**, 087004 (2003); S. Banerjee, S. Goldberg, A. Soibel, Y. Myasoedov, M. Rappaport, E. Zeldov, F. de la Cruz, C. J. van der Beek, M. Konczykowski, T. Tamegai, and V. M. Vinokur, *ibid.* **93**, 097002 (2004).
- <sup>35</sup>U. Welp, Z. L. Xiao, J. S. Jiang, V. K. Vlasko-Vlasov, S. D. Bader, G. W. Crabtree, J. Liang, H. Chik, and J. M. Xu, *Phys. Rev. B* **66**, 212507 (2002).
- <sup>36</sup>W. Vinckx, J. Vanacken, V. Moshchalkov, S. Mátéfi-Tempfli, M. Mátéfi-Tempfli, S. Michotte, L. Piraux, and X. Ye, *Physica C* **459**, 5 (2007).
- <sup>37</sup>P. Bushev, D. Bothner, J. Nagel, M. Kemmler, K. B. Konovalenko, A. Lörincz, K. Ilin, M. Siegel, D. Koelle, R. Kleiner, and F. Schmidt-Kaler, *Eur. Phys. J. D* **63**, 9 (2011).
- <sup>38</sup>M. Bibes, J. E. Villegas, and A. Barthelemy, *Adv. Phys.* **60**, 5 (2011).